

# Shedding new light on historical metal samples using micro-focused synchrotron X-ray fluorescence and spectroscopy<sup>☆</sup>

D. Grolimund<sup>a,\*</sup>, M. Senn<sup>b</sup>, M. Trottmann<sup>b</sup>, M. Janousch<sup>a</sup>, I. Bonhoure<sup>a</sup>,  
A.M. Scheidegger<sup>a</sup>, M. Marcus<sup>c</sup>

<sup>a</sup>Swiss Light Source and Waste Management Laboratory, Paul Scherrer Institute (PSI), WLG A 221, Villigen PSI CH-5232, Switzerland

<sup>b</sup>Swiss Federal Laboratories for Materials Testing and Research (EMPA), CH-8600 Dübendorf, Switzerland

<sup>c</sup>Advanced Light Source (ALS), Berkeley, CA-94720, USA

Received 3 November 2003; accepted 20 February 2004

## Abstract

Synchrotron-based micro-X-ray fluorescence (micro-XRF) and micro-X-ray absorption spectroscopy (micro-XAS) were used in the present study to obtain spatially resolved micro-scale information on elemental composition, trace element distribution, chemical speciation and oxidation state and/or mineral phase distribution within historical iron artefacts dating from the Iron Age to early Medieval Times. Large area two-dimensional trace element distribution maps and oxidation state maps with micrometer spatial resolution were required to answer open archaeological questions in the context of ancient metal processing. The first set of examples was focusing on historical weapons and included two ancient iron sword blades. The micro-XRF maps revealed a distinct, highly correlated distribution pattern of trace elements such as As, Ni, Cu and Zn. Accordingly, the number of used raw materials could be determined unambiguously and key information concerning the used ancient smithing technique were gained. Further, the ability to record—in a fast manner—large area maps with high spatial resolution ('elemental screening') led to the discovery of a hitherto unknown enhanced occurrence of selected trace elements (Cu, Zn, and Au) at the blade surface. Complementary investigations by high resolution scanning electron microscopy were able to localize these trace metals within a carbon-rich matrix may be pointing towards an artifact induced during preservation. A second set of investigated artefacts is dealing with smithing waste products and related historical processing techniques and conditions. Synchrotron-based micro-XRF and micro-XAS were used to determine the structural composition as well as the spatial variation of the predominant Fe oxidation state and corresponding crystallographic phases. The study revealed the presence of distinct domains of Fe<sup>0</sup>, Fe<sup>II</sup>O (wustite), and α-Fe<sup>III</sup>OOH (goethite), separated by sharp domain boundaries. These findings help to gain new insights concerning the nature and origin of used raw materials as well as regarding employed processing techniques during historic iron fabrication and weapon manufacturing. The study demonstrates the potential of oxidation state and mineral phase mapping based on energy selective micro-XRF maps and spectroscopic phase identification. Such a spatially resolved recording of the chemical speciation is based on X-ray absorption spectroscopy. This analytical technique is exclusive to synchrotron light sources. However, the steadily increasing number of available synchrotron-based X-ray microprobes allows nowadays for more routine utilization of such micro-XAS techniques.

© 2004 Elsevier B.V. All rights reserved.

**Keywords:** Micro X-ray absorption spectroscopy; Micro-XRF; Micro-XANES; Micro-EXAFS; Archaeology; Grazing-exit; Oxidation state mapping

## 1. Introduction

Archaeology seeks to improve our understanding of ancient cultures based on non-documentary artefacts. Knowledge related to provenance, dating, manufacturing techniques, or usage is deduced by scientific methods based on compositional and structural investigations of artefacts. Such

<sup>☆</sup> This paper was presented at the International Congress on X-Ray Optics and Microanalysis (ICXOM XVII), held in Chamonix, Mont Blanc, France, 22–26 September 2003, and is published in the special issue of *Spectrochimica Acta Part B*, dedicated to that conference.

\* Corresponding author. Tel.: +41 56 310 47 82; fax: +41 56 310 45 51.

E-mail address: Daniel.Grolimund@psi.ch (D. Grolimund).

information is required to develop an extended or refined picture about, e.g., technical capabilities, structure and development of economies, or social organization and lifestyle of ancient societies. Furthermore, conservation, restoration, and the question of authenticity rely nowadays heavily on the application of modern analytical techniques.

A wide variety of bulk (macro) analytical techniques are routinely employed in the field of archaeometry. These techniques can reveal *average* compositional, chemical, structural or morphological information of ancient materials. Evidently, each new analytical technique improved the accessibility of the historic information inherent in ancient materials [1]. By adding spatial resolution to selected bulk techniques, the development of microprobes resulted in major advancements in archaeology. In this context, synchrotron-based X-ray microprobes can be regarded as the latest extension to the available suite of micro-analytical techniques. The small source size and low emittance of new third generation synchrotron sources [2–4], in combination with recent advances in the design and production of hard X-ray focusing optics [5–10], allowed the construction of dedicated high-flux microprobe beam lines [11–22]. Key advantages of these synchrotron-based analytical facilities are the extraordinary brilliance and high photon flux, wavelength tunability, and the polarization of the synchrotron radiation. The availability of micro-focused X-ray radiation led to the development and/or improvement of various analytical microprobe techniques, including analytical, imaging, and spectroscopic tools. Some of these tools are exclusive to synchrotron facilities, e.g., X-ray Absorption Spectroscopy (XAS). XAS corresponds to a powerful collection of techniques able to provide molecular-level characterization of materials [23–27]. Most frequently used XAS techniques are X-ray Absorption Near Edge Structure (XANES) and Extended X-ray Absorption Fine Structure (EXAFS). Element-specific chemical information such as coordination or bonding environment and oxidation state can be obtained. The ability to conduct XAS experiments using X-ray microprobes adds a new dimension to the investigation of materials: Chemical speciation with micron-scale spatial resolution.

Clearly, synchrotron-based microprobes provide the possibility to characterize manifold samples in a way, which cannot be conquered with any other ‘conventional’ microprobe method. Furthermore, the characteristic properties of synchrotron radiation allows to examine complex samples in a non-destructive manner with high spatial resolution and sensitivity as well as chemical specificity—all being crucial prerequisites for investigations of archeological artefacts [28–31].

In this study we present a number of case studies applying synchrotron-based micro-X-ray fluorescence (micro-XRF), micro-XANES, as well as micro-EXAFS to iron and steel artefacts. Samples were sword blades as well as smelting slag and smithing waste in form of worked bloomery iron and hammerscale, with dating ranging from the Iron Age to early

Medieval Times. The retrieved information enables us to enlighten the nature and origin of used raw materials as well as the employed processing techniques during historic iron fabrication and weapon manufacturing.

## 2. Materials and methods

### 2.1. Samples

The historical samples available for X-ray microprobe analysis are cross-sections from two sword blades and iron slag products. All samples are originating from archeological sites located in the northern part of Switzerland. The swords are single objects found in the lake Murten BE (afterwards referred to as ‘water sword’) and a grave at Conthey-Daillon VS (‘graveyard sword’), respectively. The iron waste originates from a smithy related to the roman villa excavated near Neftenbach ZH. While the iron waste artefact dates from the Roman Times, the two weapons have been manufactured during the Late Iron Age [32,33]; cat. number 36, 105, 106 in Ref. [32]. Prior to investigation, cross-sections were obtained by sectioning and embedding a fraction of each artefact in epoxy resin followed by polishing. Initial characterization was done by classical microscopy. A limited number of point measurements by laser ablation inductively coupled plasma mass spectrometry (LA-ICP-MS) were conducted to gain preliminary information on trace element concentrations (V, Cr, Mn, P, Co, Ni, Cu, As) present in the different artefacts.

As for the iron waste products, the main interest is focused on identification and spatial distribution of different mineral/amorphous phases and related oxidation states within the ‘bulk’ iron materials. This kind of information is crucial in deciphering and understanding the process conditions operational during smithing. Concerning the sword blades, the main goal was to investigate the structure and determine the spatial distribution of key elements in order to draw conclusions regarding used raw materials as well as applied forging techniques.

### 2.2. Micro-XAS

All synchrotron-based micro-XAS investigations reported here were conducted at beamline 10.3.2 of the Advanced Light Source (ALS), Berkeley. Typical operation conditions of the ALS were 1.9 GeV and 400 to 200 mA current.

The microprobe beamline 10.3.2 is a bending magnet beamline dedicated to environmental micro-spectroscopy [22,34,35]. The beamline employs a two-step focusing strategy, first producing a 1:1 image of the source. This image acts as a secondary source which is subsequently demagnified by two elliptical mirrors aligned in a classical Kirkpatrick-Baez arrangement [36,37]. The size of the secondary source can be reduced dynamically using a slit

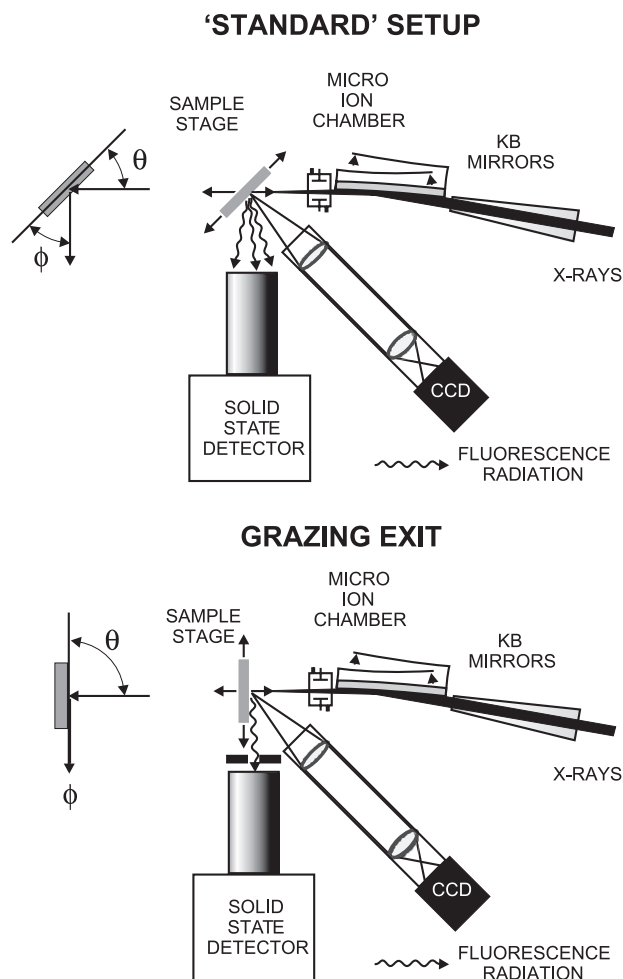


Fig. 1. Experimental setup with standard micro-XAS setup (top) and grazing-exit setup (bottom).

system. This setup allows—in a fast manner—to adjust the final X-ray spot size in the range between  $5 \times 5$  and  $16 \times 7 \mu\text{m}^2$ . The X-ray beam was monochromated by means of a fixed-exit double crystal monochromator using a pair of Si(111) crystals. Energy calibrations were carried out using standard metal foils measured in transmission. Further details regarding the beamline concept and the optical layout can be found in Refs. [34,37].

Two-dimensional X-ray fluorescence maps were collected using a fully motorized  $x$ - $y$  scanning stage. Samples were exposed to monochromatic X-ray radiation of variable energy (see below). Fluorescence emission was monitored with an energy dispersive 7-element Ge solid-state detector (Canberra). Locations of interest were selected based on micro-XRF maps, and micro-XANES as well as micro-EXAFS spectra were collected to determine the chemical speciation with spatial resolution of a few microns.

For both, micro-XRF mapping and micro-XAS, two different types of beam-sample-detector geometries were employed. First, as for the standard setup the detector is oriented  $90^\circ$  incident to the beam while the sample is mounted at a  $45^\circ$  angle. The second type of setup, which

was used for spectroscopy at the Fe K-edge on Fe-rich samples, allows the use of the grazing-exit geometry (see below). Fig. 1 provides a schematic representation of these two setups.

### 2.3. Chemical speciation mapping

The fine structure of an absorption edge reveals information on the chemical speciation of the absorber [23,24,27]. As an example, Fig. 2 shows Fe K-edge XANES spectra for three iron reference compounds having different oxidation states. The most obvious feature is a shift in the edge position depending on the oxidation state. Additional disparities can be attributed to differences in the local chemical environment (within a distance of  $\sim 5 \text{ \AA}$ ). As a result, pronounced differences in the normalized absorption can be observed at characteristic energies. These differences represent chemical contrast which can be used to record two-dimensional distribution maps of oxidation states, mineral phases, or different molecular species.

Recording multiple two-dimensional maps by tuning the excitation energy to these selected energies and subsequent logical filtering allows one to make two-dimensional chemical speciation maps. As an example of logical filtering—based on the example depicted in Fig. 2—the following condition would produce a distribution map for zero-valent iron being the predominant chemical species

$$I_{i,j}^{\text{Fe}^0} = \begin{cases} I_{i,j}(7240) & \text{if } \frac{I_{i,j}(7119)}{I_{i,j}(7240)} \in [0.5; 0.7] \cap \frac{I_{i,j}(7125)}{I_{i,j}(7240)} \in [0.8; 1.0] \\ 0 & \text{otherwise} \end{cases} \quad (1)$$

with  $i$  and  $j$  defining the matrix element (pixel), and  $I_{i,j}(x)$  corresponding to the Fe K $\alpha$  fluorescence intensity measured

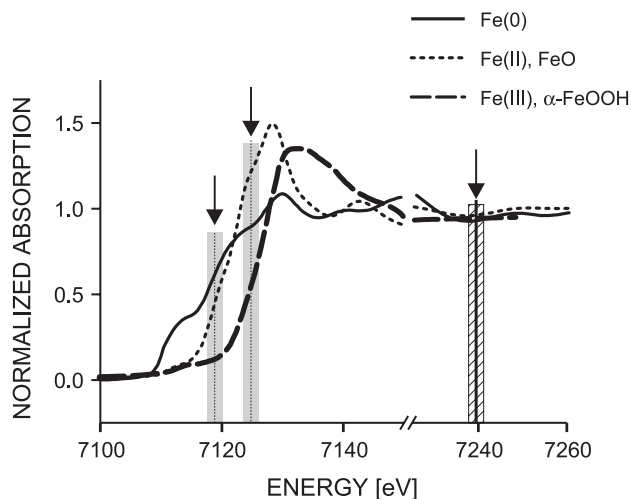


Fig. 2. XANES spectra of elemental  $\text{Fe}^0$  (solid line),  $\text{Fe}^{\text{II}}\text{O}$  (dotted line), and  $\alpha\text{-Fe}^{\text{III}}\text{OOH}$  (goethite, dashed line). The gray areas represent energy regions of high chemical contrast. For the hatched area the contrast is minimal and used for normalization.

at pixel  $ij$  for selected energies  $x$ . The corresponding interval boundary values for  $\text{Fe}^{\text{II}}$  would be [0.4;0.6] at 7119 eV and [1.1;1.3] at 7125 eV, as well as [0.0;0.2] and [0.5;0.7] for  $\text{Fe}^{\text{III}}$ , respectively.

Obviously, the robustness of this method can be enhanced by an increased number of conditions (maps recorded at energies revealing chemical contrast) but also by a careful selection of plausible reference XANES spectra used to determine the energies of highest chemical contrast. Prior to extensive chemical mapping, a comparison of micro-XANES measurements at selected locations with reference spectra can yield useful indications regarding the potential iron phases present in the sample. In the present study, the following iron mineral phases have been used as reference compounds:  $\alpha\text{-Fe}^{\text{III}}\text{OOH}$  (goethite),  $\beta\text{-Fe}^{\text{III}}\text{OOH}$  (akaganeite),  $\gamma\text{-Fe}^{\text{III}}\text{OOH}$  (lepidocrite),  $\text{Fe}_2^{\text{III}}\text{O}_3$  (hematite),  $\text{Fe}^{\text{II}}\text{Fe}_2^{\text{III}}\text{O}_4$  (magnetite),  $\text{Fe}^{\text{II}}\text{O}$  (wustite),  $\text{Fe}^{\text{II}}\text{SiO}_4$  (fayalite),  $\text{Fe}^{\text{II}}(\text{CO}_3)$  (siderite), and  $\text{Fe}^{\text{II}}(\text{Al}_2\text{O}_4)$  (hercynite).

#### 2.4. Over-absorption and grazing-exit setup

As for every other analytical technique, (micro-)XAS results can be biased by experimental artefacts or experimenter's mistakes. Related to X-ray microprobe investigations, a general and comprehensive discussion can be found in Ref. [34].

The archaeological artefacts under investigation in this study correspond to bulk samples with the absorber atom of interest present in high concentration (e.g. pure iron metal). If the sample material is concentrated and thick, the fluorescence signal to be recorded is distorted in a characteristic way, often referred to as 'over-absorption' [38–40]. As a characteristic result, the experimentally obtained XAS spectra show an apparent amplification of the pre-edge region while the fine structure amplitudes found in the post-edge region are considerably damped. As outlined by Manceau et al. [34], for highly concentrated bulk samples (quasi-infinite samples), the damping factor  $D$  diminishing the amplitude of the EXAFS signal can be expressed as

$$D = \frac{\alpha_b + \alpha_f \sin\theta / \sin\phi}{\alpha_b + \alpha_f \sin\theta / \sin\phi + \alpha_r}, \quad (2)$$

where  $\alpha_b$  and  $\alpha_r$  correspond to the background part and the resonant part, respectively, of the absorption coefficient and  $\alpha_f$  represents the absorption coefficient for the fluorescence radiation. Given a sample with the surface plane oriented perpendicular to the plane of the storage ring,  $\theta$  represents the angle between the sample surface plane and beam axis and  $\phi$  indicates the angle between surface plane and detector axis (Fig. 1).

By inspecting Eq. (2) it becomes evident that the resonant absorption part  $\alpha_r$  should be small compared to  $\alpha_b$  and/or  $\alpha_f$  in order to keep  $D$  close to 1. However, for a given absorber concentration in a highly concentrated sample, the

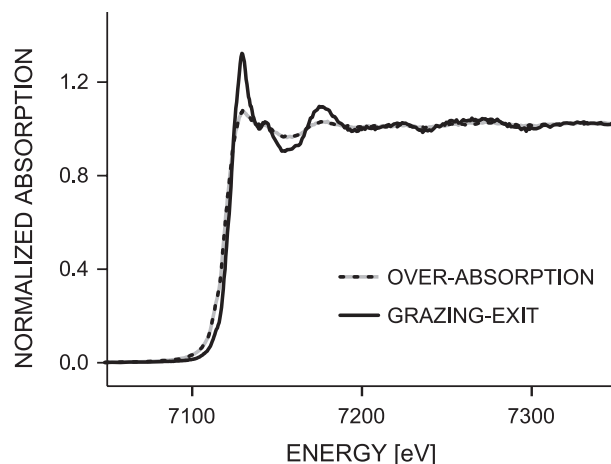


Fig. 3. Comparison between EXAFS spectra collected in grazing-exit mode (solid line) versus data recorded with standard micro-XAS setup (dotted line). The spectra measured using the standard sample geometry is subject to pronounced distortion due to 'over-absorption'.

only effective strategy to reduce the relative contribution of  $\alpha_r$  is to maximize the term  $\alpha_f \sin\theta / \sin\phi$  by minimizing the angle  $\phi$ . This corresponds to aligning the sample plane with the detector axis ( $\rightarrow$  grazing-exit setup with  $\theta \sim 90^\circ$  and  $\phi \sim 0^\circ$ , compare Fig. 1). One has to note, however, that the grazing exit strategy is limited to smooth-surfaced samples.

The phenomena related to over-absorption are illustrated in Fig. 3 for the case of an ancient bloomery iron artefact. For such samples, the local iron concentration easily exceeds 95%. Fig. 3 depicts two Fe K-edge spectra recorded at the very same spot; however, one was measured using the standard setup (subject to over-absorption), a second one employing the grazing-exit setup. While the phase information is fully consistent in both spectra, the amplification of the pre-edge region and the amplitude reduction of the extended fine structure oscillations are readily apparent. Ignoring the impact of over-absorption, the EXAFS data analysis would yield coordination numbers that are too small.

### 3. Results and discussion

#### 3.1. Structural composition of ancient sword blades: micro-XRF and micro-XAS

Fig. 4 (middle and bottom panels) shows results of micro-XRF investigations of the 'water sword' blade. As a selection, elemental distributions maps of Fe (as a contour reference), arsenic, and nickel are depicted. The incident energy was set to 13.00 keV, just below the Pb  $L_3$  edge at 13.055 keV. This energy is sufficient to excite As but not Pb, whose  $L\alpha$  fluorescence overlaps the  $K\alpha$  of As. These synchrotron-based microprobe investigations complement preceding local analysis by laser-ablation ICP-MS and investigations by means of metallographic etching [32,33]. Despite considerable effort, the data obtained by these

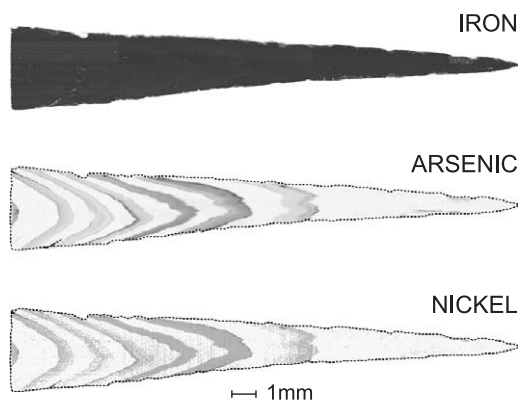


Fig. 4. Elemental distribution of Fe, As, and Ni detected by micro-XRF within a cross-section of an ancient sword ('water sword') dating from the late Iron Age. In the middle and bottom panels a dotted line is included as contour reference.

techniques turned out to be indecisive regarding the determination of the forging technique used during blade production. The main limitation arises due to the point-like character of the LA-ICP-MS measurements as well as the heterogeneity of the carbon content as observed by the etching technique. Full-field two-dimensional multi-element distribution maps are required to determine the number and type of welded raw materials unambiguously.

The micro-XRF maps revealed distinct, highly correlated distribution pattern for the trace elements As and Ni (Fig. 4b,c). Two characteristic populations of elemental correlation can be established. Delimited zones rich in As and Ni are separated by areas characterized by low concentrations of trace elements. Based on this observation one can construe that the sword was manufactured as a composite material based on (i) relatively pure iron and (ii) an iron/steel material rich in arsenic, nickel, and P (as determined by Oberhoffer etching). The regular sequence of these two composite materials is indicative of the usage of a certain piling technique, an innovation reaching the Central Swiss Alps during the middle Iron Age. The present artefact corresponds to a developed masterpiece of this technique. Manufacturing by piling techniques using alternating layers of soft and hard materials was introduced to improve the elasticity of the sword blades. The investigated sword shows a surface-to-surface banding structure. Further, as evident from Fig. 4, middle panel, the piling structure is terminated by a thin and partly preserved band of the hard iron/steel material (P and As rich) resulting in a hard cutting edge of the sword. Overall, the observed internal structure of the sword blade is indicative of exceptionally high manufacturing quality.

By inspecting the banding structure in more detail, a fine structure in the As rich layers can be established. Systematic gradients in the local As concentration—an enrichment in the direction of the last worked surface—are indicative of segregation phenomena which occurred during smithing. In addition, micro-EXAFS investigations (data not shown) reveal that arsenic is present in its reduced oxidation state

as As(III). Such complementary, molecular level information can yield important contributions to understand the processing conditions, in particular process temperature and cooling conditions.

The results of the micro-XRF analysis of the 'graveyard sword' are depicted in Fig. 5. Similar to the previous example, a composite structure could be established. However, arsenic shows a more pronounced enrichment along the welding seams. Similar enrichment of phosphorus in combination with arsenic and nickel along welding seams was observed by McDonnell [41].

Synchrotron-based micro-XRF allows for fast full-field element screening. Such a survey yielded unexpected results for the graveyard sword blade. Copper and zinc were found to be enriched at the blade surface (Fig. 5c,d). High-resolution maps (not shown) revealed a fuzzy structure of the Cu and Zn rich surface layer. The thickness was on average approximately 10–20  $\mu\text{m}$ . In order to increase the sensitivity to additional trace elements, single point micro-XRF spectra were collected at selected locations with extended exposure times. An example is shown in Fig. 6. In addition to Cu and Zn, traces of gold were occasionally found at the blade surface.

With only the micro-XRF results available, an initial working hypothesis attributed the enhanced occurrence of selected trace metals to the corrosion of the sword scabbard made out of brass and subsequent contamination of the blade surface. Alternatively, the traces of gold led to speculate about a possible surface decoration by a brass coating with gold ornaments. Complementary investigations by high resolution scanning electron microscopy (data not shown) were conducted to elucidate further the origin of the enhanced surface concentrations. The cavities of the fuzzy outer-most layer of the blade surface turned out to be filled

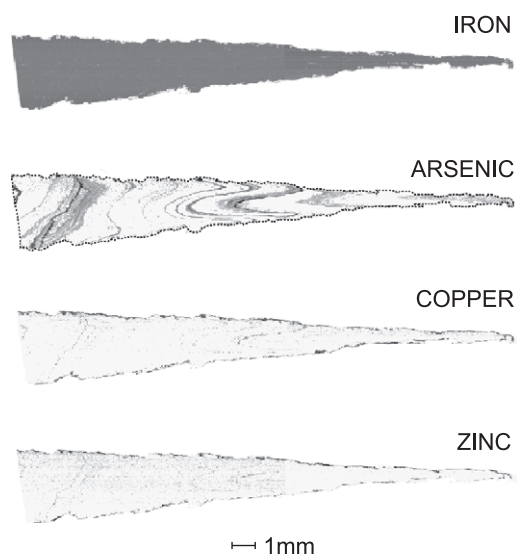


Fig. 5. Elemental distribution of Fe, As, Cu, and Zn detected by micro-XRF within a cross-section of an ancient sword ('graveyard sword') dating from the late Iron Age. In case of arsenic a dotted line is included as contour reference.

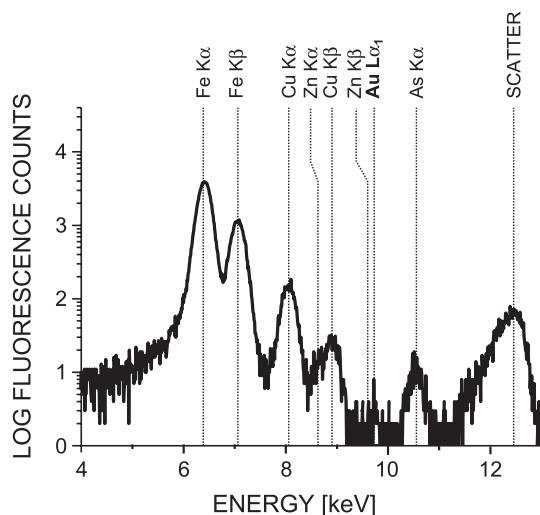


Fig. 6. X-ray fluorescence spectra collected from the surface of an ancient sword ('graveyard sword') dating from the late Iron Age. Excitation energy was set to 13.00 keV, X-ray beam size was  $5 \times 5 \mu\text{m}^2$ . Semi-logarithmic representation.

by a material rich in C, Pb, and Sn. Traces of Cu were detected, but Zn and Au were below detection limit. Such an elemental composition, however, is not characteristic for any metallic surface coating. Based on the carbon-rich matrix, the observed elemental distribution may be explained by the presence of an organic substance enriched by heavy metals. At the time of excavation, the sword was still embedded in its scabbard, which was indeed made from a non-ferrous alloy [42]. There are indications that in the past used motor oil was employed to ease the separation of metal pieces corroded together. Speculating again, such an inadequate way of preservation may be another explanation for the observed trace element distribution. Additional micro-analytical investigations are required to support either hypothesis.

### 3.2. Chemical composition of bloomery iron: oxidation state mapping

The spatial variability of the chemical speciation of iron and the distribution of associated iron mineral phases was mapped for a bloomery iron artefact dating from Roman

Times. Fig. 7 shows a schematic representation of the sample as well as the localization of the sampling area investigated by micro-XRF/XAS. The resulting oxidation state maps are shown in Fig. 8, while micro-spectroscopic results obtained at selected locations are reported in Fig. 9.

The investigated sample shows only minor evidence for mechanic processing with an unaltered porosity originating from smelting. Isolated slag inclusions can be detected. Iron with such a characteristic is often found in the inner part of "Spitzbarren" iron bars, a common form of merchandised iron at Roman Times. As sketched in Fig. 7a, the appearance of the sample suggests two types of oxidation processes. The inner part of the iron piece represents a zone of 'hot oxidation', while the outer shell corresponds to an area of 'cold oxidation' (crosshatched area). Our micro-XRF/XAS investigations covered both these zones (Fig. 7b). A micrograph is shown in Fig. 7b, while the corresponding iron fluorescence micro-XRF map is depicted in Fig. 7c. Obviously, without chemical contrast towards iron speciation, only topographic phenomena and non-iron inclusions are visible. The pattern of the chemical speciation of bulk and trace elements within such metallic artefacts, however, represent crucial information necessary to reconstruct the historic metallurgic processing.

Fig. 8 shows the result of the oxidation state mapping. The spatial distributions of the different iron oxidation states are illustrated as false-colour images. The maps have been constructed using the procedure outlined in Section 2.3. The analysis revealed clearly separated areas, each representing the predominant presence of a given iron oxidation state (Fig. 8a–c). Such 'valence islands' were found for all three oxidation states separated by less than  $100 \mu\text{m}$  (Fig. 8e). Fig. 8d depicts zones with multiple (mixed) iron valence states present within the area of one pixel ( $20 \times 20 \mu\text{m}^2$ ). As can be seen by inspecting Fig. 8e, mixed oxidation states are mainly present along phase boundaries. Such an indication of mixed iron valence could be based on either a phase with truly mixed iron valence states (e.g., magnetite,  $\text{Fe}^{\text{II}}\text{Fe}^{\text{III}}\text{O}_4$ ) or the simultaneous presence of multiple phases within a few micrometers (e.g., sharp phase boundaries). Micro-spectroscopic investigations can resolve these ambiguities.

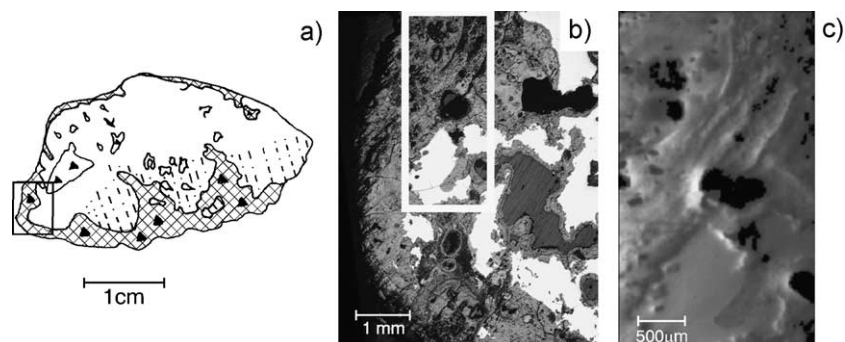


Fig. 7. Roman iron smithing waste sample. (a) Schematic representation of investigated cross-section. (b) Back-reflection micrograph. (c) Total iron distribution measured by microXRF. Iron-free areas correspond to slag inclusions or open porosity.

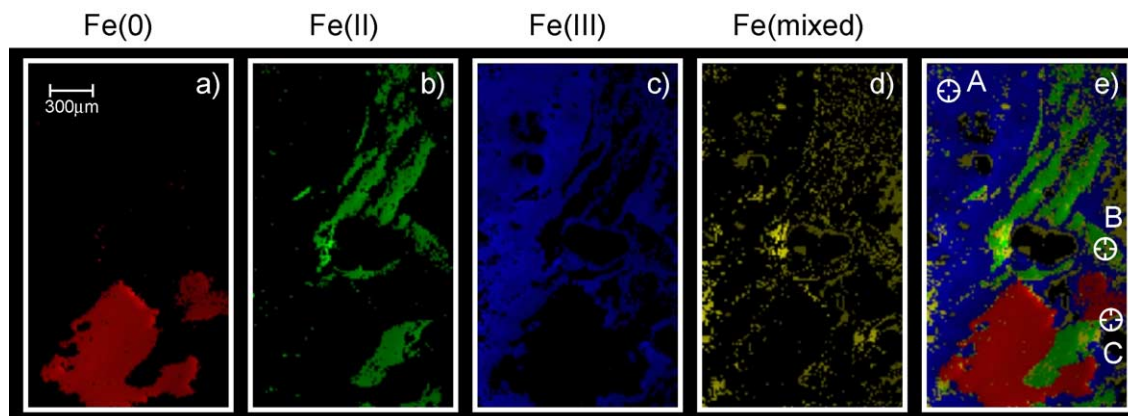


Fig. 8. Distribution of iron oxidation states within a selected area of a Roman smelting waste sample. Oxidation state maps representing areas with predominant occurrence of (a)  $\text{Fe}^0$ , (b)  $\text{Fe}^{\text{II}}$ , (c)  $\text{Fe}^{\text{III}}$ , and (d) areas with multiple iron oxidation states present. (e) Complete oxidation state map. Markers and labels indicate locations selected for micro-XANES and micro-EXAFS investigations (Fig. 9).

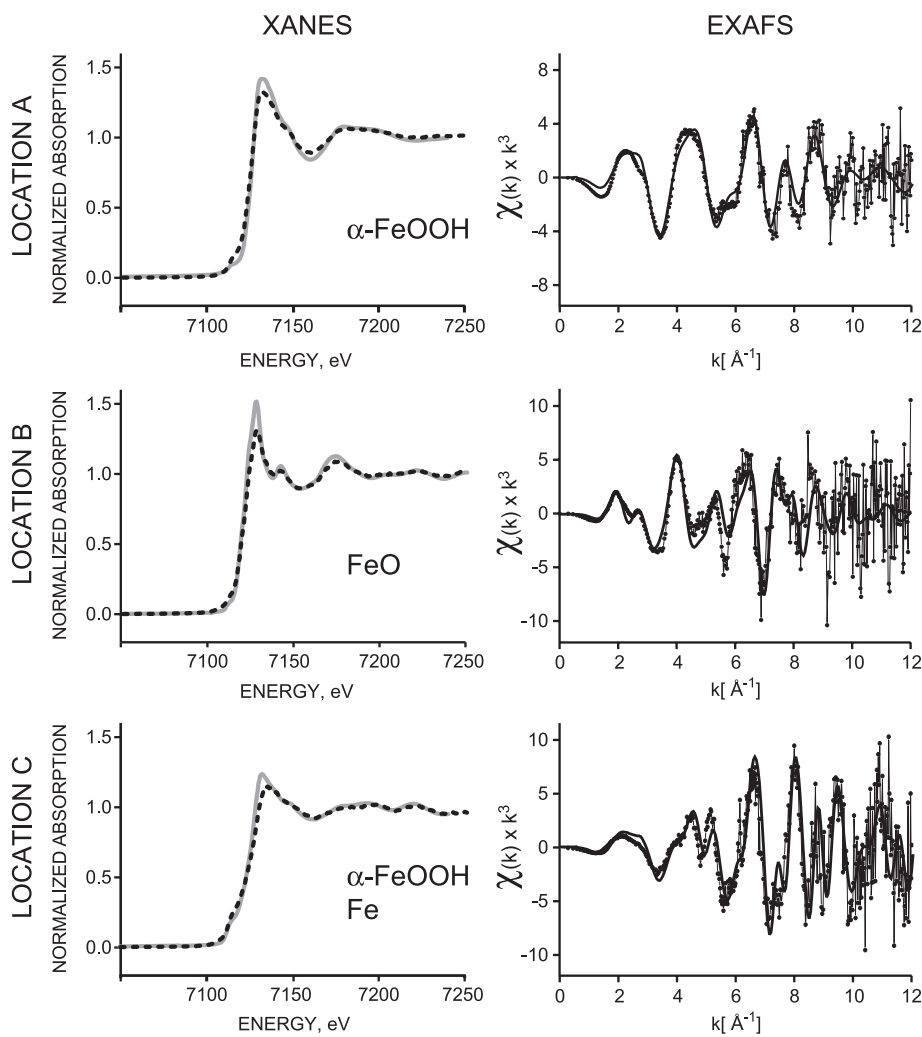


Fig. 9. Micro-XANES and  $k^2$ -weighted Fe K-edge micro-EXAFS spectra collected at three selected locations within a Roman smelting waste sample (A, B, and C; Fig. 8). Black dotted lines (micro-XANES) represent a comparison with experimental reference XANES spectra of  $\alpha\text{-Fe}^{\text{III}}\text{OOH}$  (goethite; location A),  $\text{Fe}^{\text{II}}\text{O}$  (wustite, location B), and a linear combination of elemental iron  $\text{Fe}^0$  (25%) and  $\alpha\text{-Fe}^{\text{III}}\text{OOH}$  (75%) (location C). Black solid lines (EXAFS) correspond to FEFF8 [43] simulations of  $\alpha\text{-Fe}^{\text{III}}\text{OOH}$ ,  $\text{Fe}^{\text{II}}\text{O}$ , and of a linear combination of  $\text{Fe}^0$  and  $\alpha\text{-Fe}^{\text{III}}\text{OOH}$  simulations, respectively.

Accordingly, in order to confirm the two-dimensional iron valence distribution obtained by means of oxidation state mapping and to identify the corresponding iron phase, micro-EXAFS spectra were collected at selected spots marked in Fig. 8e. Spot A appears to be an Fe(III) containing phase and spot B a phase rich in Fe(II). Spot C corresponds to an interface region.

Fig. 9 shows the XANES spectra and the  $k^3$ -weighted EXAFS spectra recorded at locations A, B, and C (see Fig. 8e). The micro-XANES spectra (Fig. 9, left panel) are compared to XANES spectra of well-characterized reference compounds measured in transmission. The experimental micro-EXAFS spectra (Fig. 9, right panel) on the other hand are compared to theoretical calculations using FEFF8 [43].

For locations A and B, there is very good agreement of the experimental data (micro-XANES and micro-EXAFS) with the spectra of goethite ( $\alpha$ -Fe<sup>III</sup>OOH; location A) and wustite (Fe<sup>II</sup>O; location B). The remaining deviations can, at least to a certain extent, be attributed to distortions of the micro-XAS spectra caused by over-absorption. Despite the usage of a grazing-exit sample alignment, a slight enhancement of the pre-edge region and a moderate damping of the post-edge fine structure is still detectable. Observed deviations are in close agreement with calculations [44]. An additional reduction of the solid angle accepted by the detector would be necessary to reduce the apparent amplitude reduction even further.

The results of the micro-spectroscopic investigations support the results obtained by the oxidation state mapping (Fig. 8). Further, goethite and wustite could be identified as the predominant iron phases present at the locations A and B, respectively. For location C, the situation is a bit more complex, since at this location different oxidation states occur on the micron scale. A comparison with various mixed valence iron minerals did not yield a satisfying match. However, a reasonable description of the experimental data (XANES and EXAFS) can be obtained, assuming the co-existence of goethite and elemental Fe<sup>0</sup> (best linear combination fits indicate 25% Fe<sup>0</sup> and 75%  $\alpha$ -Fe<sup>III</sup>OOH). Consulting the oxidation state map (Fig. 8e) one can indeed identify spot C to be located at a Fe<sup>0</sup>-Fe<sup>III</sup> boundary.

Thus, for such a complex situation too, the XANES and EXAFS data confirm the results obtained by oxidation mapping. The present example illustrates the strength of combining oxidation state mapping based on near-edge contrast with XAS experiments at selected locations. This strategy allows the determination of the spatial distribution of different chemical species within a heterogeneous sample. In the context of metallic artefacts, the spatial variability of the chemical speciation of matrix or trace elements and the distribution of associated phases correspond to the principal witness of historic metallurgical processes. Employing the presented analytical strategy based on micro-XAS fundamental information becomes available to archaeologists and metallurgists.

## 4. Conclusions

In the present study, micro-XRF and micro-XAS was used to obtain spatially resolved information on the trace element distribution and the spatial variability of the chemical speciation within historical artefacts dating from the late Iron Age to early Medieval Times.

Given the characteristic length-scale of the phenomena of interest (e.g., corrosion layers, welded layers, welding seams, chemical micro-structure of worked iron, etc.) achieving micrometer resolution is mandatory. While alternative microprobe techniques could also provide elemental distributions, the spatially resolved determination of chemical speciation is restricted to micro-XAS techniques. Molecular-level characterization, however, is often the key to decipher ancient materials.

Synchrotron-based micro-XAS and micro-XRF offer a great potential of investigating ancient samples in a non-destructive fashion with high spatial resolution. With an increasing number of available of X-ray microprobes, studies based on these techniques can be expected to play an increasing role in enlightening the technological and economic development of ancient societies.

## Acknowledgments

The Advanced Light Source (ALS) is supported by the Director, Office of Science, Office of Basic Energy Sciences, Materials Science Division, of the U.S. Department of Energy under Contract No. DE-AC03-76SF00098 at Lawrence Berkeley National Laboratory.

The Swiss National Museum, Zurich, and the Department of Archaeology, Canton of Zurich, are acknowledged for providing the historic samples and for financial support (MS).

## References

- [1] E. Ciliberto, G. Spoto, *Modern Analytical Methods in Art and Archaeology*, John Wiley & Sons, New York, 2000.
- [2] H. Wiedemann, *Synchrotron Radiation*, Springer, Berlin, 2003.
- [3] J. Als-Nielsen, D. McMorrow, *Elements of Modern X-ray Physics*, John Wiley & Sons, New York, 2001.
- [4] D.M. Mills (Ed.), *Third-Generation Hard X-ray Synchrotron Radiation Sources*, John Wiley & Sons, New York, 2002.
- [5] G.E. Ice, J.S. Chung, J.Z. Tischler, A. Lunt, L. Assoufid, Elliptical X-ray microprobe mirrors by differential deposition, *Rev. Sci. Instrum.* 71 (2000) 2635–2639.
- [6] B.X. Yang, M. Rivers, W. Schildkamp, P.J. Eng, Geocars micro-focusing Kirkpatrick-Baez mirror bender development, *Rev. Sci. Instrum.* 66 (1995) 2278–2280.
- [7] O. Hignette, G. Rostaing, P. Cloetens, A. Rommeveaux, W. Ludwig, A.K. Freund, Submicron focusing of hard X-rays with reflecting surfaces at the ESRF, *SPIE 2000*: Berlin, 2000.
- [8] M.R. Howells, D. Cambie, R.M. Duarte, S. Irick, A.A. MacDowell, H.A. Padmore, T.R. Renner, S. Rah, R. Sandler, Theory and practice of elliptically bent X-ray mirrors, *Opt. Eng.* 39 (2000) 2748–2762.

- [9] C. David, B. Nohammer, H.H. Solak, F. Glaus, B. Haas, A. Grubelnik, A. Dolocan, E. Ziegler, O. Hignette, M. Burghammer, B. Kaulich, J. Susini, J.H.H. Bongaerts, J.F. van der Veen, Diffractive soft and hard X-ray optics, *J. Phys.*, IV 104 (2003) 171–176.
- [10] A. Snigirev, V. Kohn, I. Snigireva, B. Lengeler, A compound refractive lens for focusing high-energy X-rays, *Nature* 384 (1996) 49–51.
- [11] P. Chevallier, P. Dhez, F. Legrand, A. Erko, Y. Agafonov, L.A. Panchenko, A. Yakshin, The Lure-IMT X-ray fluorescence photon microprobe, *J. Trace Microprobe Tech.* 14 (1996) 517–539.
- [12] R. Devoti, F. Zontone, C. Tuniz, F. Zanini, A synchrotron radiation microprobe for X-ray-fluorescence and microtomography at elettra-focusing with bent crystals, *Nucl. Instrum. Methods, B* 54 (1991) 424–428.
- [13] S. Hayakawa, S. Goto, T. Shoji, E. Yamada, Y. Gohshi, X-ray microprobe system for XRF analysis and spectroscopy at spring-8 BL39XU, *J. Synchrotron Radiat.* 5 (1998) 1114–1116.
- [14] M.R. Howells, J.B. Hastings, Design considerations for an X-ray microprobe, *Nucl. Instrum. Methods* 208 (1983) 379–386.
- [15] K. Janssens, L. Vincze, F. Adams, K.W. Jones, Synchrotron-radiation-induced X-ray-microanalysis, *Anal. Chim. Acta* 283 (1993) 98–110.
- [16] M.L. Rivers, S.R. Sutton, J.V. Smith, A synchrotron X-ray-fluorescence microprobe, *Chem. Geol.* 70 (1988) 179.
- [17] F. Vanlangevelde, G.H.J. Tros, D.K. Bowen, R.D. Vis, The synchrotron radiation microprobe at the SRS, Daresbury (UK) and its applications, *Nucl. Instrum. Methods, B* 49 (1990) 544–550.
- [18] Y. Suzuki, F. Uchida, Hard X-ray microprobe with total-reflection mirrors, *Rev. Sci. Instrum.* 63 (1992) 578–581.
- [19] S. Bohic, A. Simionovici, A. Snigirev, R. Ortega, G. Deves, D. Heymann, C.G. Schroer, Synchrotron hard X-ray microprobe: fluorescence imaging of single cells, *Appl. Phys. Lett.* 78 (2001) 3544–3546.
- [20] A. Somogyi, M. Drakopoulos, B. Vekemans, L. Vincze, A. Simionovici, F. Adams, Effects of beamline components (undulator, monochromator, focusing device) on the beam intensity at ID18F (ESRF), *Nucl. Instrum. Methods, B* 199 (2003) 559–564.
- [21] M. Newville, S. Sutton, M. Rivers, P. Eng, Micro-beam X-ray absorption and fluorescence spectroscopies at GSECars APS beamline 13ID, *J. Synchrotron Radiat.* 6 (1999) 353–355.
- [22] M.A. Marcus, A.A. MacDowell, R. Celestre, E. Domning, K. Franck, A. Manceau, G. Morrison, T. Miller, H.A. Padmore, R.E. Sublett, Beamline 10.3.2 at ALS: a hard X-ray microprobe for environmental and material sciences, *J. Synchrotron Radiat.* 11 (2004) 239–247.
- [23] B.K. Teo, D.C. Joy (Eds.), *EXAFS Spectroscopy: Techniques and Applications*, Plenum Press, New York, 1981.
- [24] D.C. Koningsberger, R. Prins, *X-ray Absorption, Principles, Applications, Techniques of EXAFS, SEXAFS and XANES*, John Wiley & Sons, New York, 1988.
- [25] H. Saisho, Y. Gohshi, *Applications of Synchrotron Radiation to Materials Analysis*, Elsevier Health Science, 1996.
- [26] G.E. Brown Jr., in: M.F. Hochella, A.F. White (Eds.), *Mineral Water Interface Geochemistry*, vol. 23, Mineralogical Society of America, Washington, DC, 1990, pp. 309–363.
- [27] J. Stoehr, *NEXAFS Spectroscopy*, Springer, Berlin, 1996.
- [28] G. Harbottle, B.M. Gordon, K.W. Jones, Use of synchrotron radiation in archaeometry, *Nucl. Instrum. Methods, B* 14 (1986) 116–122.
- [29] C. Lahanier, G. Amsel, C. Heitz, M. Menu, H.H. Andersen, *Nucl. Instrum. Methods, B* 14 (1986) 1-ff.
- [30] K. Janssens, G. Vittiglio, I. Deraedt, A. Aerts, B. Vekemans, L. Vincze, F. Wei, I. Deryck, O. Schalm, F. Adams, A. Rindby, A. Knochel, A. Simionovici, A. Snigirev, Use of microscopic XRF for non-destructive analysis in art and archaeometry, *X-ray Spectrom.* 29 (2000) 73–91.
- [31] P. Dillmann, P. Populus, P. Chevallier, P. Fluzin, G. Beranger, A. Firsov, Microdiffraction coupled with X-ray fluorescence microprobe. application in archaeometry, *J. Trace Microprobe Tech.* 15 (1997) 251–262.
- [32] M. Senn Bischofberger, *Das Schmiedehandwerk in der nordalpinen Schweiz von der Eisenzeit bis ins Frühmittelalter*, in: *Internationale Archäologie. Naturwissenschaft und Technik*, Bd., vol. 5, Verlag Marie Leidorf GmbH, Rahden, Germany, 2004.
- [33] M. Senn, W. Devos, Some news about the chemical composition of bloomery iron materials, *Archaeometallurgy in Europe: Milan, Italy*, vol. 1, 2003, pp. 17–26.
- [34] A. Manceau, M.A. Marcus, N. Tamura, in: P. Fenter, N.C. Sturchio (Eds.), *Applications of Synchrotron Radiation in Low-Temperature Geochemistry and Environmental Science*, vol. 49, Mineralogical Society of America, Washington, DC, 2002, pp. 341–428.
- [35] M.A. Marcus, <http://xraysweb.lbl.gov/uxas/>.
- [36] P. Kirkpatrick, A.V. Baez, Formation of optical images by X-rays, *J. Opt. Sci. Am.* 38 (1948) 766–774.
- [37] A.A. McDowell, C.M. Lamble, R.S. Celestre, J.R. Patel, H.A. Padmore, Progress towards sub-micron hard X-ray imaging using elliptically bent mirrors and its implications, *SPIE Conference on X-ray Microfocusing: Applications and Techniques: San Diego, CA*, vol. 3449, 1998, pp. 137–144.
- [38] W. Frentrop, D. Schroder, R. Manzke, Correction of self absorption on Xas measurements in fluorescence mode, *J. Phys.*, IV 7 (1997) 509–510.
- [39] J. Goulon, C. Gouloninnet, R. Cortes, J.M. Dubois, On experimental attenuation factors of the amplitude of the EXAFS oscillations in absorption, reflectivity and luminescence measurements, *J. Phys.* 43 (1982) 539–548.
- [40] L. Troger, E. Zschech, D. Arvanitis, K. Baberschke, Quantitative fluorescence EXAFS analysis of concentrated samples—correction of the self-absorption effect, *Jpn. J. Appl. Phys.* 32 (1993) 144–146.
- [41] J. McDonnell, in: B.G. Scott, H. Cleere (Eds.), *The Crafts of the Blacksmith*, UISPP, Belfast, 1984, pp. 87–89.
- [42] M.-R. Sauter, *Vallesia* 5 (1950) 87.
- [43] A.L. Ankudinov, B. Ravel, J.J. Rehr, S.D. Conradson, Real space multiple scattering calculations of XANES, *Phys. Rev.*, B 58 (1998) 7565.
- [44] D. Haskel, FLUO: Correcting XANES for Self-absorption in Fluorescence Measurements, UWXAFS Project, University of Washington, Seattle, 1999, <http://depts.washington.edu/uwxafs>.